nature communications

Article

https://doi.org/10.1038/s41467-025-63577-x

Lanthanum-assisted lattice anchoring of iridium in Co_3O_4 for efficient oxygen evolution reaction in low-iridium water electrolysis

Received: 18 February 2025

Accepted: 21 August 2025

Published online: 31 August 2025

Check for updates

Zhuoming Wei[1], Yunxuan Ding[1,2] ✉, Weili Shi[1], Feiyang Zhang[1], Yuxiang Song[1], Xin Cui[1], Yu Guo[1,2], Licheng Sun[1,2,3], Qike Jiang[4] & Biaobiao Zhang[1,2,3] ✉

The use of single-atom catalysts is an effective way to reduce the amount of iridium in proton exchange membrane water electrolysis (PEM-WE). However, conventional methods can only obtain surface-loaded single atoms or clusters which cannot meet the needs of high current density and stability. In this study, assisted by lanthanum-doping-induced ion exchange, we realize atomically anchoring iridium within the Co_3O_4 lattice. The lattice anchored iridium in lanthanum-doped Co_3O_4 exhibits higher atomic dispersion, a larger average coordination number, and an elevated oxidation state. This improvement stimulates the oxide path mechanism (OPM), resulting in enhanced activity (236 mV at 10 mA cm^{-2}) and stability (1000 h at 10 mA cm^{-2}). Impressively, our catalyst demonstrates notable performance in a PEM electrolyzer with an iridium mass loading of just 0.2 mg_{Ir} cm^{-2}, achieving a low cell voltage of 1.61 V at 1.0 A cm^{-2} and maintaining stable operation for over 1000 h. This work presents an effective strategy for fabricating low-noble-metal-loading catalysts with enhanced efficiency for PEM-WE.

Hydrogen (H_2) is a promising carbon-free energy source due to its high energy density and environmental friendliness, positioning it as a key energy carrier for achieving future carbon neutrality[1]. Among the various technologies for hydrogen production, proton exchange membrane water electrolysis (PEM-WE) stands out for its low contact resistance, broad power range, and ability to couple with the intermittent power from renewable electricity, making it more favorable compared to established alkaline water electrolysis technology[2]. However, the large-scale viability of PEM-WE is hindered by the high cost (~ US$60,670 per kilogram) and scarcity (approximately 7 tons per year) of iridium (Ir), the only feasible catalytic materials for the acidic oxygen evolution reaction (OER). It requires high mass loading of Ir-based catalysts (1.0–3.0 mg_{Ir} cm^{-2}) at the anode[3–6]. To break through the limitation of Ir, significant research efforts have focused on reducing Ir loading in membrane electrode assembly (MEA) modules. Previous strategies have focused on mixing Ir with other elements, such as constructing Ir-based multi-component oxides and alloys, or incorporating Ir with other materials into heterogeneous or core-shell structures[7–10]. Although these catalysts maintain activity to a certain extent while achieving lower Ir content, none of them exhibit comparable performance to rutile IrO_2 in terms of both OER activity and stability under PEM-WE conditions[11]. Significant challenge remains

[1]Center of Artificial Photosynthesis for Solar Fuels and Department of Chemistry, School of Science and Research Center for Industries of the Future, Westlake University, Hangzhou, China. [2]Institute of Natural Sciences, Westlake Institute for Advanced Study, Hangzhou, China. [3]Division of Solar Energy Conversion and Catalysis at Westlake University, Zhejiang Baima Lake Laboratory Co., Ltd., Hangzhou, China. [4]Instrumentation and Service Center for Physical Sciences, Westlake University, Hangzhou, China. ✉e-mail: dingyunxuan@westlake.edu.cn; zhangbiaobiao@westlake.edu.cn

in reducing the amount of Ir in catalysts while ensuring their durability for industrial applications in PEM-WE[12].

Consequently, immobilizing a small amount of Ir species on acid-resistant substrates has emerged as a promising strategy for developing OER catalysts with low Ir loading[13]. In this context, several Ir-based single-atom catalysts (SACs) have been developed for acidic OER, including Ir-MnO_2, TiO_xN_y-Ir, Ir-$NiCo_2O_4$ and Ir-$MnCo_2O_{4.5}$[11,14–18]. Some of these catalysts exhibit extremely low overpotential at current density of 10 mA cm^{-2} and high mass activity for acidic OER. However, most of these reported low content Ir-based catalysts show limited activity and stability at high current levels (>200 mA cm^{-2}), which is far from satisfying the demand of the practical PEM-WE[19]. As a classic method for preparing supported SACs, conventional ion exchange methods can only obtain surface-loaded single atoms or clusters which face challenges such as low mass loading, atomic dispersion maintenance, excessive oxidation and corrosion under harsh reaction conditions, limiting their industrial application in PEM-WE[20,21]. In order to enhance the catalytic performance of SACs, it is important to strengthen the interaction between the precious metal single atom and the support[22]. Compared to surface-adsorbed single atoms, SACs with lattice-anchored atoms in the surface lattices of metal oxide, are expected to have a more complete coordination environment and lower surface energy (Fig. 1)[21]. Additionally, these SACs exhibit stronger interatomic synergies between the support's metallic elements and the single atoms, demonstrating the potential for maintaining dispersed atomic sites with sustained activity[23]. It is of great importance and challenge to develop lattice anchoring methods to obtain stable low-content Ir-based single atom OER catalysts.

In this work, we realized the lattice anchoring of Ir single atoms into the Co_3O_4 nanoparticles by a lanthanum (La)-doping assisted ion exchange method. La incorporation drives efficient ion exchange with Ir species, enabling atomic-level lattice doping rather than surface adsorption of Ir atoms or clusters, obtaining the LaIr-Co_3O_4 catalyst. This strategy reduces the oxidation state of the Co_3O_4 support while increasing the valence state of the anchored Ir atoms, thus reducing excessive oxidation of Co_3O_4 support and enhancing the activity of the atomic Ir species by stronger metal-support interactions. The lattice anchored atomic Ir favors the oxide path mechanism (OPM) reaction pathway alongside adjacent Co. The LaIr-Co_3O_4 catalyst expresses notable performance in a PEM electrolyzer, achieving stable operation for 1000 h at a current density of 1.0 A cm^{-2} with a low Ir loading of ~0.2 mg cm^{-2}. This LaIr-Co_3O_4 catalyst allows the amount of Ir loading to be reduced by >90% compared with the present commercial level (~2 mg cm^{-2}). This work provides insights for the precise design of robust, atomic-scale supported catalysts.

Results

Synthesis and basic structure

Ir-Co_3O_4 and LaIr-Co_3O_4 were synthesized by thermal ion exchange of Co_3O_4 and La-doped Co_3O_4, which were obtained from the calcination of cobalt-based zeolitic imidazolate framework (ZIF-67) and La-doped ZIF-67 precursors, respectively. The cobalt-based ZIF-67 nanocrystals precursor (Fig. S1a) was synthesized using a triethylamine (TEA) assisted nucleation-growth separation method. The incorporation of TEA as a crystallization accelerator enabled burst nucleation to obtain uniform monodisperse nanocrystals, further minimizing the size and reducing the preparation time of ZIF-67[24]. La^{3+} was introduced into the synthetic solution to obtain La-doped ZIF-67. La^{3+} was selected as the dopant due to its strong attraction for binding hydroxyl radicals on the surface of cobalt oxide[25]. Additionally, its ionic radius of 1.06 Å, the largest among the lanthanides, is significantly larger than that of Co^{3+} (0.65 Å), which is expected to create distortion doping sites to Co_3O_4. EXAFS analysis (Table S1) at the La L_3-edge quantitatively validated this configuration, showing a distorted octahedral coordination (CN = 5.1 ± 0.3, La-O distance R = 2.58 ± 0.012 Å), consistent with the surface segregation mechanism of large-radius ions doped in Co_3O_4, alleviating lattice distortion through surface relaxation effects thus serving as sites to promote ion exchange[26]. Figure S1b shows single-atom characteristics formed by the surface doping tendency of La. After calcination, a thermal ion exchange method was carried out to load atomic Ir onto Co_3O_4 and La-doped Co_3O_4 to form Ir-Co_3O_4 and LaIr-Co_3O_4, more details are shown in Supplementary Information. Notably, from the ICP-OES result (Table S2), the mass fraction ratio of La/Co in LaIr-Co_3O_4 (10.21%) significantly decreased compared to La-Co_3O_4 (4.85%) after ion exchange, while the mass loading of Ir in LaIr-Co_3O_4 is higher than Ir-Co_3O_4 (pure Co_3O_4 after ion exchange) with the same ion exchange reaction condition. This phenomenon is likely attributed to the larger ionic radius of La^{3+} (1.06 Å) compared to Ir^{3+} (0.68 Å), which is poorly matched within the Co_3O_4 lattice. The higher charge density of Ir^{3+}, along with its involvement of *d* orbitals in bonding, facilitates its incorporation into the Co_3O_4 lattice and substitution of La^{3+}, resulting in strong ion exchange between the lattice-doped La^{3+} in Co_3O_4 and the Ir^{3+} in solution. This behavior explains the partial leaching of La^{3+} in LaIr-Co_3O_4. As for Ir-Co_3O_4, the ion exchange between Co^{3+} in Co_3O_4 and Ir^{3+} in solution is thermodynamically difficult, thus Ir^{3+} is mainly loaded on the surface of Co_3O_4 in the form of chemically adsorbed rather than doped into the lattice of Co_3O_4 through ion exchange. For this conjecture, La-doped Co_3O_4 was immersed in a 5 mM KCl (keep the same Cl^- concentration) with the same reaction conditions as ion exchange as a comparison. The ICP-OES analysis (KCl-La-Co_3O_4) confirmed minimal dissolution of La^{3+} after immersion (Table S2), suggesting that La^{3+} remains relatively stable when the solution lacks Ir^{3+} to trigger ion exchange.

The basic structure of Ir-Co_3O_4 and LaIr-Co_3O_4 was characterized by x-ray diffraction (XRD), scanning electron microscopy (SEM), and transmission electron microscopy (TEM). Powder XRD confirmed the chemical phase of Ir-Co_3O_4 and LaIr-Co_3O_4 only corresponding to cobalt spinel oxide, indicating the atomic-level loading of Ir species (Fig. 2a). Broadened XRD peaks indicate that LaIr-Co_3O_4 has a lower

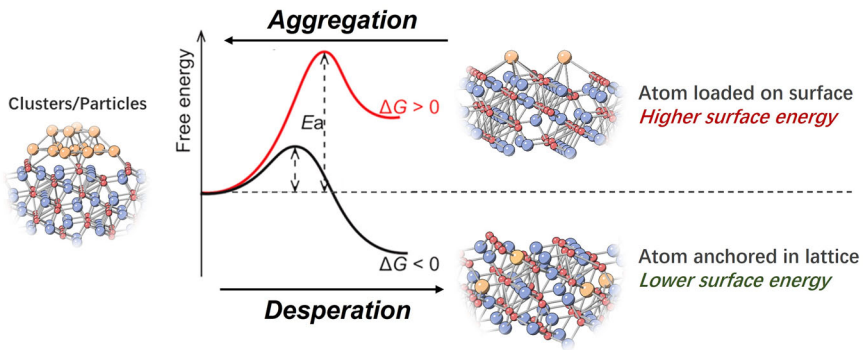

Fig. 1 | Schematic illustration of free-energy diagram two types of Ir single atom on oxide support. Orange: Precious metal atoms (e.g., Ir). Blue: Metal atoms of support (e.g., Fe, Co, Ni, Mn); Red: Lattice oxygen atoms.

https://doi.org/10.1038/s41467-025-63577-x

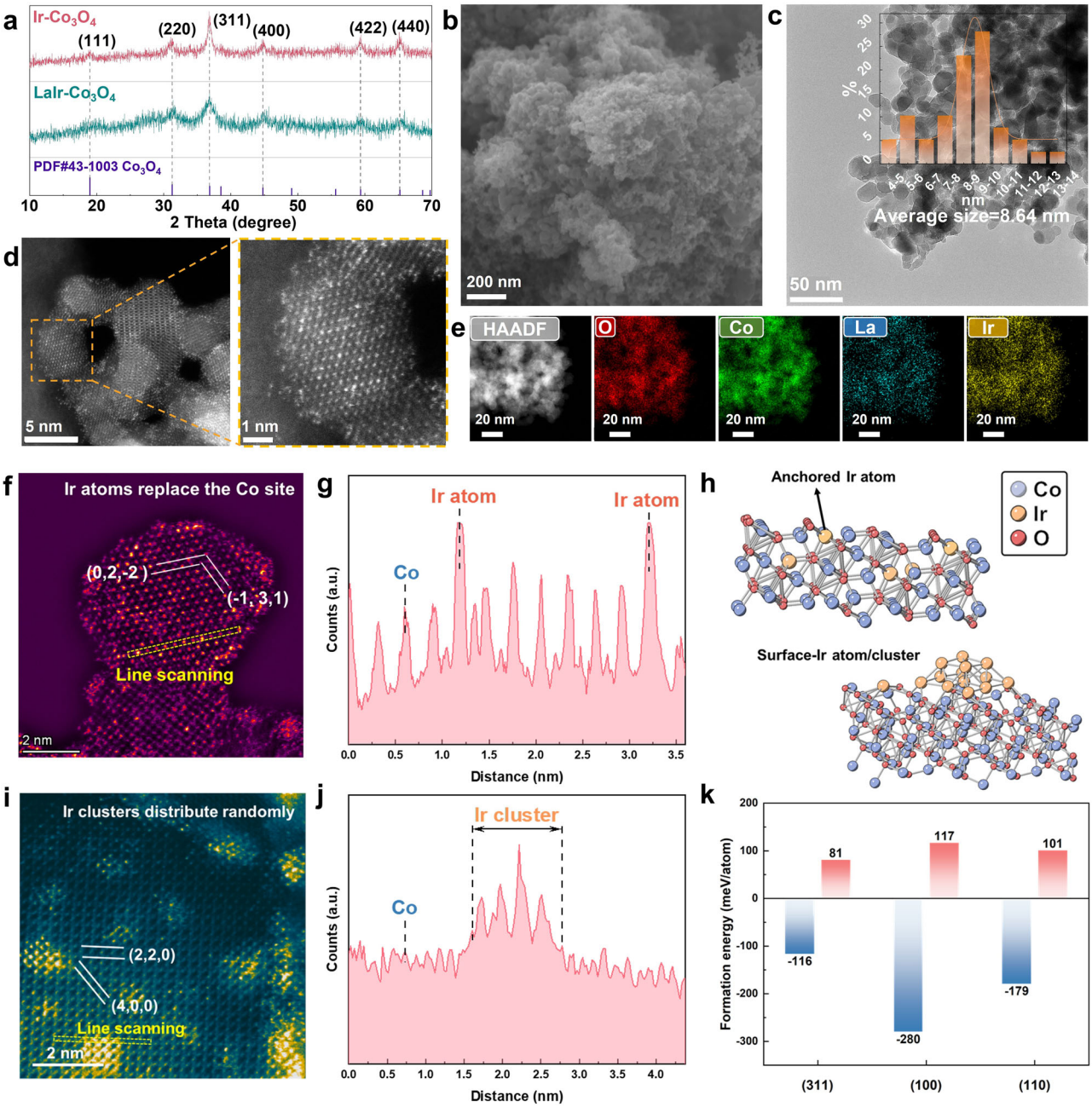

Fig. 2 | Characterisation of LaIr-Co_3O_4 and Ir-Co_3O_4 nanoparticles. a XRD patterns of Ir-Co_3O_4 and LaIr-Co_3O_4. **b** SEM image of LaIr-Co_3O_4. **c** TEM image of LaIr-Co_3O_4 (inset: size distribution of nanoparticles). **d** HAADF-STEM image of LaIr-Co_3O_4. **e** HAADF-STEM image of LaIr-Co_3O_4 and corresponding elemental mapping. **f** HAADF-STEM image of the LaIr-Co_3O_4 and **g** corresponding line-scan intensity profiles highlighted by yellow dashed boxes. **h** Structure diagram of lattice anchored Ir single atoms in Co_3O_4 (LaIr-Co_3O_4) and the surface-loaded Ir cluster on Co_3O_4 (Ir-Co_3O_4). **i** HAADF-STEM image of Ir-Co_3O_4 and **j** corresponding line-scan intensity profiles highlighted by yellow dashed boxes. **k** Formation energies for Ir^{3+} substituting La^{3+} and Co^{3+} in La-Co_3O_4 and Co_3O_4 (311), (100), and (110) facets, respectively.

crystallinity and smaller particle size. Similarly, high-resolution scanning transmission electron microscopy (HRTEM) images and corresponding FFT images (Fig. S2a, b) further confirmed more polycrystalline and less crystalline nature of LaIr-Co_3O_4 compared with Ir-Co_3O_4. SEM combined TEM images (Fig. 2b, c) demonstrate the uniform nanoparticle structure (~8.64 nm) of LaIr-Co_3O_4. In contrast, the Ir-Co_3O_4 has a larger average size of 15 nm (Fig. S3), which is consistent with the result of XRD. Furthermore, aberration-corrected high-angle annular dark-field scanning transmission electron microscopy (HAADF-STEM; Figs. 2d and S4a) confirms the atomic isolation of Ir single atoms (scattered bright dots) in the obtained LaIr-Co_3O_4. In contrast, atomic Ir species tend to aggregate into nano-clusters on the surface of Ir-Co_3O_4 (Fig. S4b) due to the lack of lattice coordination binding of chemically adsorbed Ir species. Energy dispersive X-ray spectroscopy (EDS) elemental mapping further confirmed the successful incorporation of La and the loading of Ir (Fig. 2e). HAADF-STEM images obtained at different magnifications and multiple regions verify the homogeneity of Ir single-atom distribution (Fig. S5).

Lanthanum-assisted lattice anchoring of iridium

In order to further explore the effect of La doping towards the anchoring of atomic Ir through ion exchange, the fine atomic structure was further investigated. As illustrated in Figs. 2f and S6, the atomic resolution HAADF-STEM and corresponding FFT images of a single

LaIr-Co_3O_4 nanoparticle revealed that Ir atoms are located in the same columns as the Co atoms on the (0 2 − 2) and (−1 3 1) crystal planes of Co_3O_4, indicating that the Ir atoms replace Co sites in the Co_3O_4 lattice[14]. Since La doping replaces the six-coordinated Co^{3+} site as verified by EXAFS fitting parameters (Table S1) and it has a strong ion exchange effect toward Ir^{3+}, Ir atoms were anchored in the lattice of Co_3O_4, forming these ordered single atoms by this ion exchange process.

To gain deeper insights into the formation of Co_3O_4 catalysts with Ir lattice dopants, density functional theory (DFT) calculations were conducted. To assess the feasibility of the LaIr-Co_3O_4 formation, the formation energies of Ir^{3+} replacing La^{3+} in La-Co_3O_4 and Ir^{3+} replacing Co^{3+} in Co_3O_4 were calculated (Fig. 2k). The calculated formation energies for Ir^{3+} substituting doped La^{3+} in Co_3O_4 (311), (100), and (110) facets are −116, −280, and −179 meV/atom, respectively, indicating the spontaneous exothermic processes. In contrast, it is challenging for the direct substitution of Co^{3+} in Co_3O_4 (311), (100), and (110) facets by Ir^{3+}, as reflected by the endothermic processes with the formation energies of 81, 117, and 101 meV/atom, respectively. Therefore, the synthesis of Ir-anchored Co_3O_4 through the substitution of surface La^{3+} with Ir^{3+} is thermodynamically more favorable than the direct exchange of surface Co^{3+} with Ir^{3+}. This strong ion exchange effect explains the formation of Ir single atoms that anchored in the lattice of LaIr-Co_3O_4 (as illustrated in Fig. 2h). The corresponding line-scan (marked by a dotted yellow dash line in Fig. 2f) intensity profile also prove the distribution of individual lattice anchored Ir atoms as illustrated in Fig. 2g. The uniform distribution of lattice anchored Ir atoms on different single nanoparticles proves the uniformity of Ir single atoms (Fig. S7). As previously discussed, without the ion exchange induced by La, Ir loaded on Ir-Co_3O_4 primarily exist as surface-adsorbed species, which tend to aggregate into nanoclusters to minimize surface energy. HAADF-STEM image and line-scan intensity profile (Fig. 2i, j) of Ir-Co_3O_4 revealed the atomic cluster structure Ir species on the (2 2 0) and (4 0 0) crystal planes along with the schematic of crystal structure (Fig. 2h).

Coordination and electronic structure

To verify the bulk homogeneity of this lattice anchored Ir atomic structure at a more macroscopic level, the local atomic coordination environments of Co and Ir in LaIr-Co_3O_4 and Ir-Co_3O_4 were determined using extended X-ray absorption fine structure (EXAFS) spectroscopy. As shown in Fig. 3a, both LaIr-Co_3O_4, Ir-Co_3O_4 and Co_3O_4 standard samples show three distinct interatomic distances characteristic of Co −O, octahedral Co_{oct}–Co_{oct}, and tetrahedral Co_{tet}–Co_{tet} pairs, leading to three peaks in Co *K*-edge FT-EXAFS spectra, respectively[27]. The Ir L_3-edge FT-EXAFS spectra (Fig. 3b) of LaIr-Co_3O_4 and Ir-Co_3O_4 display two interatomic distances corresponding to Ir−O and Ir−Co_{oct} scattering, respectively[27]. Bond lengths of Ir-Ir bond (2.707 Å) in Ir-foil different from the Ir-Co bond in LaIr-Co_3O_4 (2.973 Å) and Ir-Co_3O_4 (2.966 Å) implying no metallic Ir species in the second shell scattering. The longer Ir-Co distances in LaIr-Co_3O_4 preliminary indicates a slight lattice expansion caused by Ir being anchored and replacing Co sites into the lattice. The fitted curves of the k_2-weighted Co *K*-edge and Ir L_3-edge EXAFS spectra of all samples in Figs. S8 and S9, corresponding fitting parameters are listed in Tables S3 and S4. The fitting coordination number (CN) of three Co interatomic distances of two samples were summarized in Table S3 and shown in Fig. 3c. The lowest average CN value of Co in LaIr-Co_3O is agreeing with a more defects generated from the doping of large ionic radius La^{3+} and the cation vacancies left by the leaching of La^{3+} during the ion exchange process. Notably, the fitting CN for Ir-O and Ir-Co scattering in LaIr-Co_3O_4 are higher compared to those in Ir-Co_3O_4 (Fig. 3d). This indicates that more Ir atoms are doped in the surface lattice following La-induced ion exchange, resulting in a more fully coordinated environment, as opposed to the surface-adsorbed isolated Ir species in Ir-Co_3O_4. The CN value of Ir-O scattering in LaIr-Co_3O_4 could be defined as a six-coordination structure (Table S4), which corresponds to octahedral units, reasonably suggests that Ir atoms preferentially occupy the Co_{oct} positions rather than the Co_{tet} sites, which is also consistent with the conclusion we have discussed previously that La^{3+} doping replaces Co^{3+} sites and then exchanges with Ir^{3+} [28]. Meanwhile, the CN value of Ir-Co pairs in LaIr-Co_3O_4 (2.7), compared to that in Ir-Co_3O_4 (1.1), is closer to the CN value of Co_{oct}-Co_{oct} coordination of these two samples (3.5 and 4.9), further indicating more substitution of Ir atoms with Co^{3+} sites in LaIr-Co_3O_4. Moreover, the coordination environment of Ir in LaIr-Co_3O_4 and Ir-Co_3O_4 was further confirmed through wavelet transformation (Fig. 3e, f). The results indicate a more pronounced second-shell domain for Ir-Co scattering with a local maximum at R = 2.6 Å and k = 8.1 $Å^{-1}$ in LaIr-Co_3O_4, also supporting more substitution of Co sites by Ir atoms and enhancing the wavelet transformation signal. Quite different k values (8.1 $Å^{-1}$) of Ir-Co scattering compared to Ir-Ir scattering in Ir-foil (11.8 $Å^{-1}$, Fig. S10) further recognize the Ir anchored structure rather than Ir cluster. In conclusion, the analysis of synchrotron radiation results confirmed that the atomic-level Ir species in the lattice of LaIr-Co_3O_4 exhibit a more complete coordination environment, verifying the lattice anchored single-atoms structure.

This lattice anchored atomic Ir is likely to produce stronger metal-support interaction, leading to electron rearrangement between atomic Ir and Co_3O_4 support[29]. The influence of this special coordination environment on the electronic structure and oxidation state was further investigated using high-resolution x-ray photoemission spectroscopy (XPS). The surface Co 2*p* XPS spectra (Fig. 3g) of LaIr-Co_3O_4 and Ir-Co_3O_4 show a peak at the binding energy near 779.9 eV which is assigned to Co $2p_{3/2}$, including Co^{III} and Co^{II}. The peak located around 60.2 eV is attributed to Co $3p$[30]. The decrease in the Co^{III}/Co^{II} ratio of LaIr-Co_3O_4 (Table S5) is ascribed to the occupied octahedral sites by substituted Ir atoms, as revealed by EXAFS, along with electron transfer from Ir atoms to Co sites[28]. The Ir 4*f* XPS spectra (Fig. 3h) of LaIr-Co_3O_4 exhibit an upshift of 0.21 eV and 0.22 eV in Ir $4f_{7/2}$ and Ir $4f_{5/2}$, respectively, compared to that of Ir-Co_3O_4. This further verifies the partial electron transfer from Ir to Co sites and indicates a stronger interaction between lattice anchored Ir atoms and the Co_3O_4 support.

This interaction leads to an increase in the valence state of Ir, thereby enhancing the activity of the Ir sites. The charge density differences and Bader charge analysis have been performed to quantify charge transfer between Ir and Co_3O_4. As shown in Fig. S11a, b, electrons are transferred from Ir to Co_3O_4 in both LaIr-Co_3O_4 and Ir-Co_3O_4 (311) surfaces, leading to the oxidation of Ir ions. Notably, the Ir depletes more electrons in LaIr-Co_3O_4 than in Ir-Co_3O_4. Specifically, Bader charge analysis reveals that Ir transfers 1.54 |e| to LaIr-Co_3O_4, which is 0.33 |e| more than the 1.21 |e| transferred to the Ir-Co_3O_4, indicating a higher oxidation state of Ir in LaIr-Co_3O_4 compared to Ir-Co_3O_4. This electron interaction between Co and Ir is further supported by X-ray absorption near edge structure (XANES) spectra. The Co *K*-edge XANES spectra of LaIr-Co_3O_4 and Ir-Co_3O_4 (Fig. 3i) both display electronic structures similar to that of Co_3O_4. The displacement of the white line suggests a lower oxidation state of the Co_3O_4 support in LaIr-Co_3O_4[5], matched with the XPS results. The relative position and intensity of the white line peaks energy in the Ir L_3-edge XANES corresponds to the transition from occupied 2*p* to empty 5*d* states, which is highly sensitive to the valence of 5*d* transition metal[31,32]. As shown in Fig. 3j, the Ir L_3-edge XANES spectra shows that the Ir species of both LaIr-Co_3O_4 and Ir-Co_3O_4 are oxidized with chemical states between +3 and +4. One can observe that the white line peak of LaIr-Co_3O_4 is stronger and upshifted to higher energy relative to Ir-Co_3O_4. The results are consistent with the XPS analysis, further confirming that La doping facilitates the embedding of Ir atoms into the lattice of Co_3O_4 during ion exchange. This stronger metal-support interaction is presumed to enhance the activity and stability of the catalyst.

https://doi.org/10.1038/s41467-025-63577-x

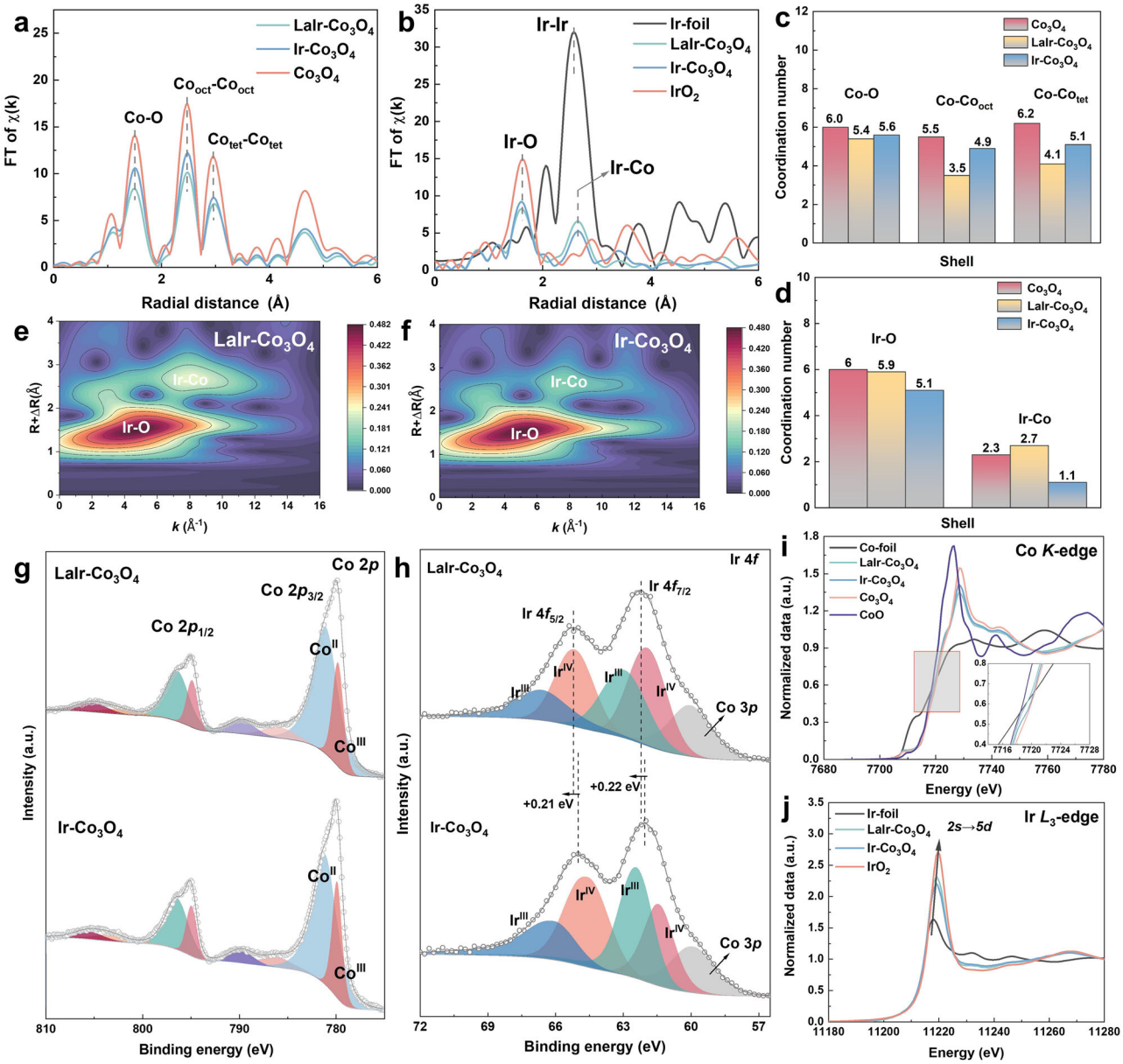

Fig. 3 | Coordination environment and electron transfer analysis. Fourier transforms of the EXAFS spectra at the Co *K*-edge (**a**) of LaIr-Co_3O_4, Ir-Co_3O_4 and Co_3O_4 and Ir L_3-edge (**b**) of LaIr-Co_3O_4, Ir-Co_3O_4 and Co_3O_4. EXAFS fitting coordination number at the Co *K*-edge (**c**) of LaIr-Co_3O_4, Ir-Co_3O_4 and Co_3O_4. EXAFS fitting coordination number at the Ir L_3-edge (**d**) of LaIr-Co_3O_4, Ir-Co_3O_4 and Co_3O_4.WT-EXAFS of LaIr-Co_3O_4 (**e**) and Ir-Co_3O_4 (**f**) at the Ir L_3-edge. High-resolution XPS spectra of Co 2*p* (**g**) and Ir 4*f* (**h**) for LaIr-Co_3O_4 and Ir-Co_3O_4. Normalized XANES spectra of Co *K*-edge (**i**) and Ir L_3-edge (**j**) for LaIr-Co_3O_4 and Ir-Co_3O_4.

The XPS depth profile analysis provided more evidence for the distinct structural distribution of Ir species between LaIr-Co_3O_4 and Ir-Co_3O_4 catalysts. As shown in Fig. S11c, the Ir 4*f* signal intensity in Ir-Co_3O_4 exhibits a progressive enhancement with increasing Ar^+ sputtering time, indicative of surface-enriched Ir clusters being gradually exposed and enhancing the signal through depth-dependent etching. This phenomenon suggests the existence of aggregated Ir species predominantly localized in the near-surface region. In striking contrast, LaIr-Co_3O_4 (Fig. S11d) demonstrates remarkably consistent Ir 4*f* intensities across successive etching cycles, maintaining low and consistent signal strength throughout the depth profiling process. This observation confirms the formation of atomically dispersed Ir species that are uniformly distributed within the surface and subsurface layers of the support. Additionally, the O 1*s* spectra (Fig. S11e, f) of both LaIr-Co_3O_4 and Ir-Co_3O_4 display binding energies corresponding to surface-adsorbed H_2O, hydroxyl groups (*OH), and lattice oxygen[33]. Due to the increased defect states induced by La doping, the O 1*s* spectra of LaIr-Co_3O_4 show a lower concentration of lattice oxygen (M–O bonds) compared to Ir-Co_3O_4, with concentrations of 61.1% and 66.2%, respectively (Table S5).

Electrochemical activity

The OER performance of all prepared samples and commercial IrO_2 (c-IrO_2) were evaluated using linear sweep voltammetry (LSV) in a 0.5 M H_2SO_4 electrolyte at room temperature. As shown in Fig. 4a, impressively, LaIr-Co_3O_4 shows greatly improved electrocatalytic activity compared to the Ir-Co_3O_4 and c-IrO_2, with overpotentials of only 236 mV required to achieve the current density of 10 mA cm^{-2}. The LSV curve of LaIr-Co_3O_4 without iR compensation was also plotted in Fig. S12, showing the influence of the resistance of the three-electrode

https://doi.org/10.1038/s41467-025-63577-x

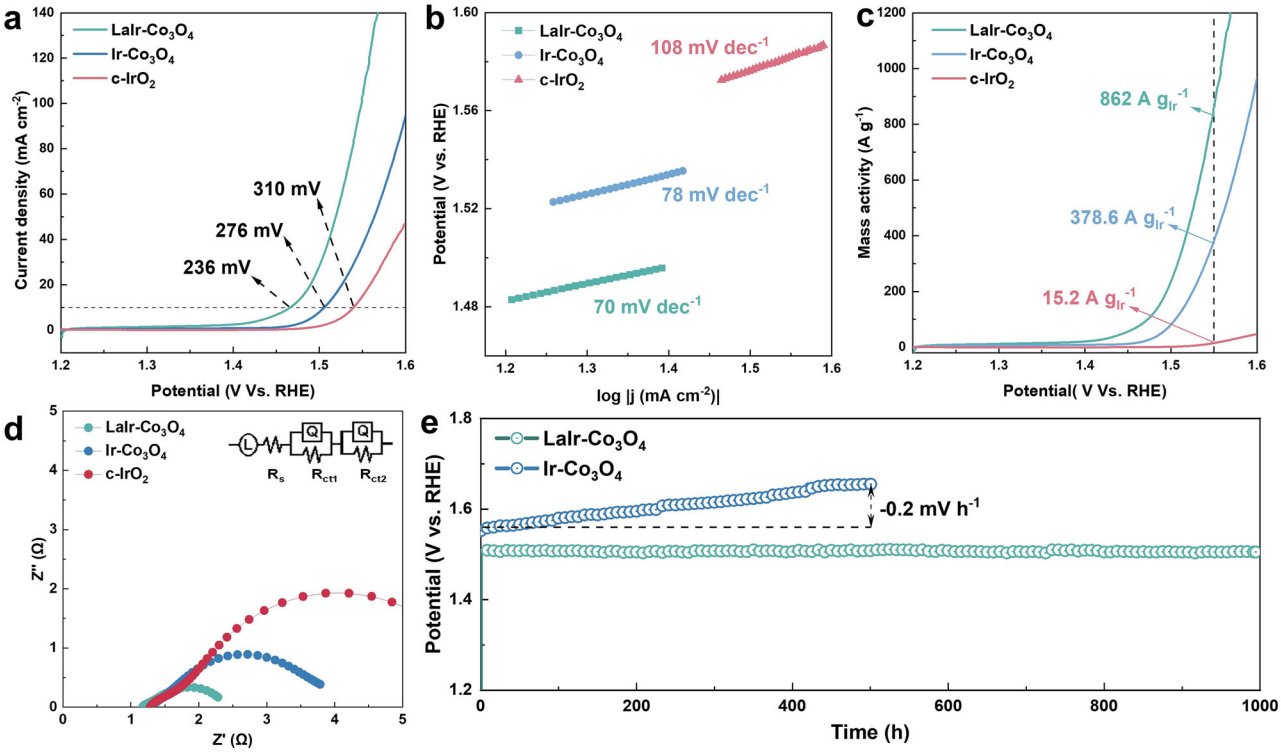

Fig. 4 | OER electrochemical performances in three-electrode system. a LSV curves (scan rate: 5 mV s^{-2}) after iR compensation (90%) with mass loading of 1.2 mg cm^{-2}. **b** Corresponding Tafel slopes. **c** Corresponding mass-activity curves. **d** Nyquist plots at 1.53 V Vs. RHE. **e** Stability test of three-electrode systems at 10 mA cm^{-2}.

test system on revealing the intrinsic activity of the catalyst. Meanwhile, the corresponding Tafel plot for LaIr-Co_3O_4 has a slope of only 70 mV dec^{-1} (Fig. 4b), which is smaller than that of Ir-Co_3O_4 (78 mV dec^{-1}) and c-IrO_2 (108 mV dec^{-1}). This lower Tafel slope suggests that the kinetics of the O–O bond formation (rate-determining step) are enhanced in LaIr-Co_3O_4, indicating the presence of a more favorable reaction pathway, such as the OPM pathway[34]. The electrochemical activity of the catalyst, normalized to the Ir content (Fig. 4c), shows that LaIr-Co_3O_4 exhibits high mass activity, being double that of Ir-Co_3O_4 and 57 times higher than that of commercial IrO_2. The turnover frequency (TOF) analysis (Table S6) demonstrated the same trend of intrinsic activity: the LaIr-Co_3O_4 catalyst exhibits the fastest TOF of 0.59 s^{-1}, which is almost 2 and 2.42 times faster than the values of Ir-Co_3O_4 and c-IrO_2 catalysts, respectively. The promoted intrinsic activity can be explained by excellent kinetics of direct O–O coupling of OPM mechanism (verified in the followed mechanism investigating section), which is even comparable to some reported designed Ru-based catalyst that followed AEM mechanism (Table S7). This enhancement is attributed to the higher intrinsic activity of the more independently dispersed Ir single atoms on LaIr-Co_3O_4. The improved electrocatalytic properties of the LaIr-Co_3O_4 were further confirmed by electrochemical impedance spectroscopy (EIS) data (Fig. 4d). Based on the fitted equivalent circuit, the R_{ct1} of the first tiny semicircle typically represents the mass transfer process on the substrate electrode, which has minimal relevance to the catalytic reactions. The second, larger semicircle corresponds to the charge transfer resistance of the reaction occurring on the catalyst's surface (R_{ct2})[35]. As a result, LaIr-Co_3O_4 exhibited significantly lower charge transfer resistance compared to Ir-Co_3O_4 and c-IrO_2, indicating superior charge transfer capabilities. The electrochemical specific surface area (ECSA) was derived from electrochemical double-layer capacitance (C_{dl}) (Fig. S13). LaIr-Co_3O_4 exhibits the highest ECSA, attributed to its smaller particle size. This increased surface area allows for more effective utilization of the anchored Ir atoms, thereby maximizing the catalytic activity. Subsequently, the long-term stability of the two as prepared electrocatalysts was evaluated via continuous chronopotentiometry tests. As shown in Fig. 5e, LaIr-Co_3O_4 maintained consistent stability in the three-electrode system E_{j10} value during the 1000 h of the test without any decrease. In sharp contrast, Ir-Co_3O_4 decays at a rate of 0.2 mV h^{-1} during continuous electrolysis of 500 h. To further confirm the stability of LaIr-Co_3O_4, the chronopotentiometry (CP) test was also carried out at 100 mA cm^{-2} (Fig. S14a). The LaIr-Co_3O_4 catalyst can still work stably for more than 100 h with negligible attenuation. The comparison of LSV curves before and after 100 mA cm^{-2} CP test shows that the performance of the LaIr-Co_3O_4 catalyst after CP test slightly declines at low potentials, but its performance at high potentials tends to approach that before the CP test (Fig. S14b).

We further calculated the stability number (S-number) for both catalysts based on the amounts of dissolved Ir and Co in the electrolyte after 60 h of continuous operation. LaIr-Co_3O_4 exhibits significantly higher S-number values than Ir-Co_3O_4 for both metals, with a striking threefold enhancement in the Ir-specific S-number (Fig. S14c). The results demonstrate that the lattice-anchored Ir atoms in LaIr-Co_3O_4 exhibit substantially enhanced leaching resistance compared to surface-loaded Ir species on Ir-Co_3O_4, while concurrently stabilizing the Co_3O_4 support. Notably, compared to state-of-the-art Ir-based catalysts[36–40], the stability of LaIr-Co_3O_4 even better (Fig. S14d).

Investigating O–O bond formation mechanism

In the previous study, the direct O–O radical coupling for O_2 evolution of oxide path mechanism (OPM) pathways that tend to occur at heteronuclear bimetallic sites have been verified to have better reaction kinetics than conventional adsorbate evolution (AEM) mechanism[34,41]. It also has no destruction of lattice oxygen as in the lattice oxygen-mediated mechanism (LOM) pathway. Since the LaIr-Co_3O_4 has more lattice coordination Ir single atoms, more Ir-Co heteronuclear bimetallic sites may be conducive to the occurrence of the OPM mechanism rather than the isolated dispersed Ir nanoclusters in Ir-Co_3O_4.

https://doi.org/10.1038/s41467-025-63577-x

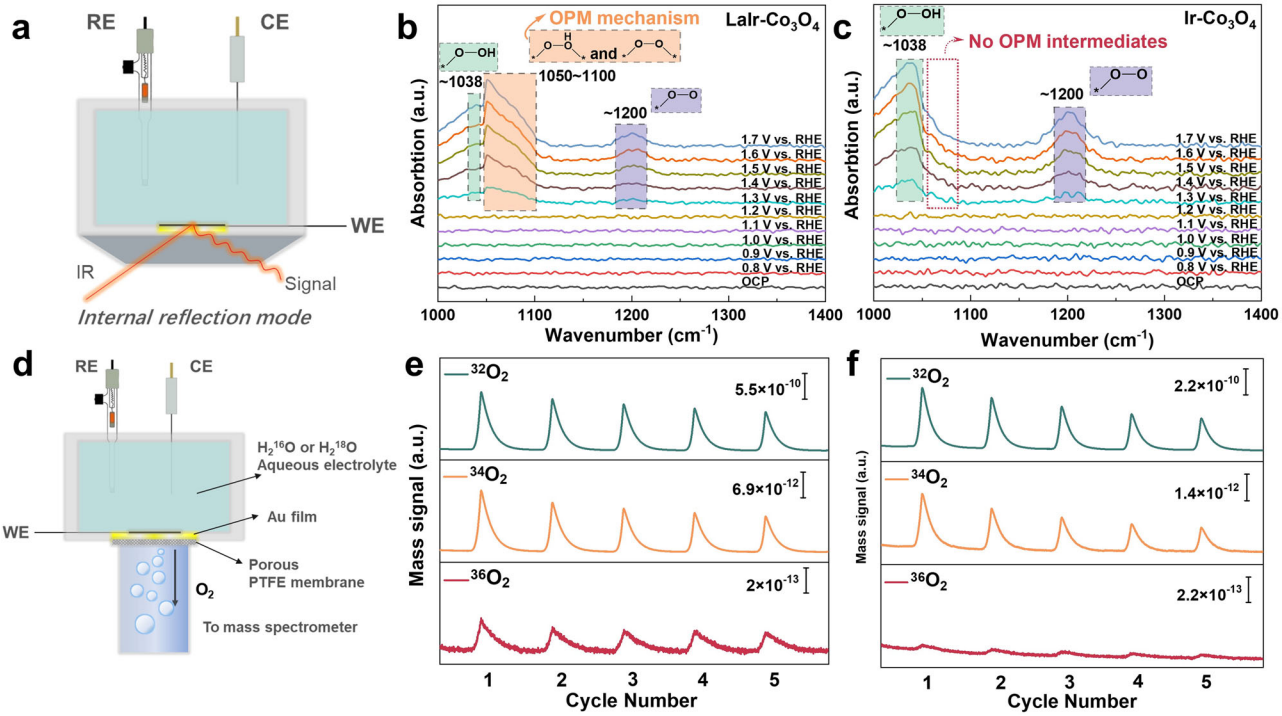

Fig. 5 | Operando ATR-SEIRAS and DEMS measurements. Schematic illustration **a** of in-situ attenuated total reflectance surface-enhanced infrared absorption spectroscopy (ATR-SEIRAS, Internal reflection mode). Operando ATR-SEIRAS measurements in the range of 1000–1400 cm^{-1} at various applied potentials for (**b**) LaIr-Co_3O_4 and (**c**) Ir-Co_3O_4, all potentials were normalized against reversible hydrogen electrode. Schematic illustration (**d**) of operando differential electrochemical mass spectrometry (DEMS). DEMS signals of O_2 products for (**e**) ^{18}O-surface labeled LaIr-Co_3O_4, and (**f**) ^{18}O-surface labeled Ir-Co_3O_4 in the electrolyte using $H_2{}^{16}O$ as solvent.

Therefore, electrochemistry in-situ ATR-SEIRAS spectroscopy (Fig. 5a) was performed to identify reaction intermediates and to elucidate the effect of lattice anchored Ir single atoms on reaction mechanism during OER process. As shown in Fig. 5b, c, upon reaching the polarization region at the anode potential, a pair of distinct absorption peaks at 1038 cm^{-1} and 1200 cm^{-1} was observed, in contrast to the spectrum obtained under open-circuit potential (OCP) conditions for both LaIr-Co_3O_4 and Ir-Co_3O_4. This indicates the production of oxygen intermediates. These absorption peaks can be identified as *OOH (1038 cm^{-1}) and *OO (1200 cm^{-1}) intermediates, formed prior to the release of O_2 from the AEM pathways[15,29]. Interestingly, a broadened peak ranging from 1050 to 1100 cm^{-1} was observed exclusively for LaIr-Co_3O_4. This peak can be attributed to the oxygen bridges between metal sites in the OPM-type oxygen evolution reaction, as reported in recent literature[42,43]. This finding strongly supports that La doping induces ion exchange, causing atomic Ir to be doped in the surface lattice of Co_3O_4, which could promote the occurrence of the OPM mechanism compared with isolated Ir nanoclusters in Ir-Co_3O_4.

To provide further validation of the OPM mechanism in LaIr-Co_3O_4, operando differential electrochemical mass spectrometry (DEMS) combined with isotope labeling was employed (Fig. 5d). XPS studies have shown that both catalysts have a rich amount of surface oxygen adsorbates OH_{ads} (Fig. S11e, f). The catalysts were first placed in 0.5 M H_2SO_4 with $H_2{}^{18}O$ as solvent for catalytic cycling to label the surface adsorbed OH_{ads} with ^{18}O, then washed and operated in a normal electrolyte 0.5 M H_2SO_4 with $H_2{}^{16}O$ as solvent to collect gas signal. If the OPM mechanism is active in LaIr-Co_3O_4, surface-bound species containing ^{18}O would likely combine to generate $^{36}O_2$, whereas no $^{36}O_2$ formation would be expected from AEM mechanism (Figs. S15 and S16)[41]. The DEMS results aligned well with these predictions (Fig. 5e, f). The LaIr-Co_3O_4 which follows the OPM mechanism, continually produced $^{32}O_2$, $^{34}O_2$ and $^{36}O_2$ during the five LSV cycles. In contrast, Ir-Co_3O_4 with isolated Ir nanoclusters structure primarily generated $^{32}O_2$ and $^{34}O_2$ with minute quantity of $^{36}O_2$, demonstrating the dominant position of AEM mechanism occurred in Ir-Co_3O_4. Furthermore, the distinct responses of catalysts to TMA^+ addition provide critical insights into their OER pathways. For commercial RuO_2, a well-documented LOM-dominated catalyst[44,45], the significant activity suppression upon TMA^+ addition aligns with the proposed mechanism where TMA^+ cations interact with free peroxo-like intermediates (O_2^{2-}) generated during lattice oxygen oxidation, thereby blocking the LOM pathway (Fig. S17a)[46]. In contrast, La-Co_3O_4 exhibit negligible sensitivity to TMA^+, strongly suggesting an AEM-dominated process (Fig. S17b). Similarly, surface-loaded Ir in Ir-Co_3O_4 likely stabilizes *OOH intermediates via conventional AEM steps without triggering lattice oxygen release (Fig. S17c).

Differently, the Ir lattice-anchoring structure in LaIr-Co_3O_4 may promote direct O–O coupling (M-OO-M) via the OPM. In OPM, the O_2^{2-} intermediates remain surface-bound during radical coupling, rendering TMA^+ less effective in suppressing activity compared to LOM[47]. The LSV curve of LaIr-Co_3O_4 shows only a very weak inhibiting effect after adding TMA^+ (Fig. S17d). Given that we have shown the doping of La does not cause the LOM mechanism to occur, and that the introduction of Ir single atoms has also been reported to stabilize lattice oxygen[14,48]. This weak attenuation can be attributed to the very small number of O_2^{2-} radicals released in the OPM path being captured by TMA^+ and inhibiting the activity. To further assess the kinetic feasibility of the reaction pathways, the transition states of the O-O coupling process for LOM and OPM were simulated via DFT calculations. As shown in Fig. S18, the activation barrier for O–O coupling process in OPM is 0.40 eV, which is significantly lower than the 1.15 eV observed in LOM pathway. The stable lattice oxygen undergoes a more challenging process when attacked by the oxygen radical. In contrast, the coupling of two oxygen radicals on the LaIr-Co_3O_4 (311) surface is more facile. Thus, the O–O coupling step is kinetically more favorable through the OPM mechanism. In conclusion, both operando and TMA^+ experiment

https://doi.org/10.1038/s41467-025-63577-x

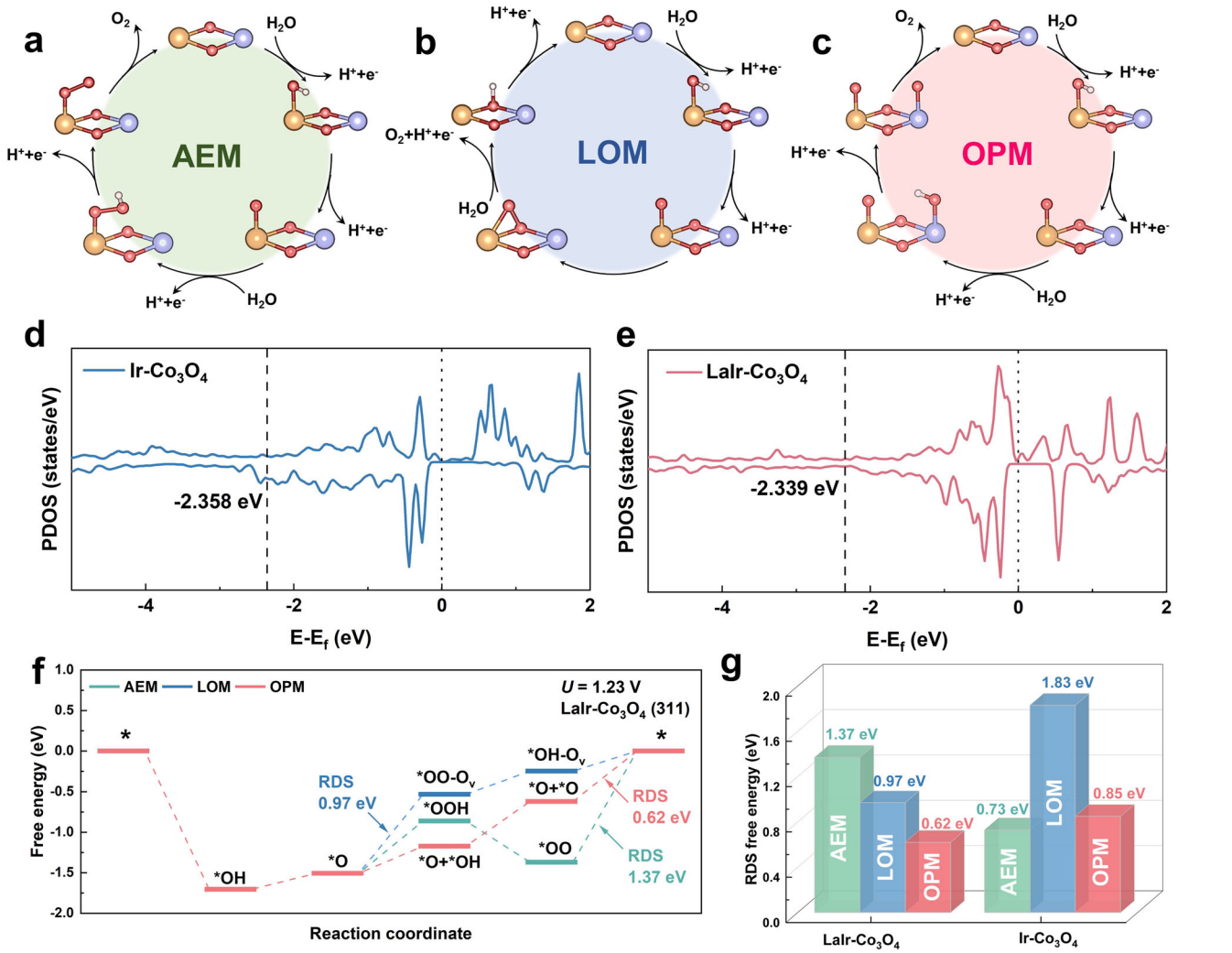

Fig. 6 | DFT calculations to reveal the advantages of the OPM path in LaIr-Co_3O_4. Schematic illustration of OER mechanisms: **a** AEM, **b** LOM, and **c** OPM. PDOS and *d*-band center of Ir 4*d* for **d** Ir-Co_3O_4 (−2.358 eV) and **e** LaIr-Co_3O_4 (−2.339 eV). **f** Free energy diagrams of different OER pathways on the LaIr-Co_3O_4 (311) surface at $U = 1.23$ V vs. RHE. **g** Comparison of the reaction free energy for the RDS of different catalytic pathways on LaIr-Co_3O_4 and Ir-Co_3O_4 (311) surfaces.

combined with theoretical calculations successfully identified the reaction intermediates from the OPM-type OER path in LaIr-Co_3O_4. Thus, we propose that La dopants serve as structural initiators that enable lattice anchoring of Ir, which in turn promotes the OPM pathway during OER through Ir-Co synergy in LaIr-Co_3O_4, as supported by the operando measurements.

DFT calculations

DFT calculations were employed to further investigate the OER mechanism on LaIr-Co_3O_4 and Ir-Co_3O_4 (311) surfaces. Compared to the Co site, the Ir site with a stronger adsorption for the oxygen species on both surfaces acts as the active site in the OER mechanism. Given the different O−O coupling processes, three mechanisms for the OER are identified, including AEM, LOM, and OPM. As shown in Fig. 6a–c, a H_2O molecule first undergoes a proton-coupled electron transfer (PCET) step and adsorbs at the Ir site to form *OH, followed by another PCET step to generate Ir-*O. The AEM involves a water nucleophilic attack (WNA) step to form *OOH, which is then deprotonated to release O_2. The LOM proceeds via an intermolecular coupling mechanism (I2M) between an adsorbed oxygen radical and a bridging oxo group (lattice oxygen) to form *OO-O_v, which releases O_2 with the introduction of *OH at the oxygen vacancy site (*OH-O_v). For the OPM, another H_2O molecule adsorbs at the adjacent Co site via continuous PCET steps to form Co-*O. Subsequently, the O−O coupling occurs between the Ir-*O and the Co-*O, followed by the O_2 release.

Moreover, projected density of states (PDOS) calculations of the 4*d* orbital for Ir show increased electron states near the Fermi level in LaIr-Co_3O_4 compared to Ir-Co_3O_4, suggesting enhanced electrical conductivity (Fig. 6d, e). Additionally, the *d*-band center of Ir in LaIr-Co_3O_4 is closer to the Fermi level than in Ir-Co_3O_4, facilitating the adsorption of intermediate species. Specifically, the adsorption free energies ($U = 0$ V) of *OH, *O, and *OOH on LaIr-Co_3O_4 (311) surface are −0.47, 0.95, and 2.83 eV, respectively (Fig. 6f), which are more stable than those on Ir-Co_3O_4 (311) surface, with values of 0.37, 1.45, and 3.41 eV at 0 V (Fig. S19). Combining with charge analysis (Fig. S11a, b), the higher oxidation state of the Ir active site in LaIr-Co_3O_4 (311) surface leads to a stronger adsorption ability of key OER intermediates, which is beneficial for increasing the coverage of these intermediates and enhancing the catalytic activity. Furthermore, the reaction free energies for the rate-determining step (RDS) of AEM, LOM, and OPM on LaIr-Co_3O_4 and Ir-Co_3O_4 (311) surfaces are illustrated in Fig. 6g, showing that OER on LaIr-Co_3O_4 prefers the OPM pathway with a reaction free energy of 0.62 eV, while OER on Ir-Co_3O_4 prefers AEM pathway with a reaction free energy of 0.73 eV. This result further suggests that LaIr-Co_3O_4 exhibits higher OER activity than Ir-Co_3O_4 through OPM reaction path, consistent with experimental observations.

https://doi.org/10.1038/s41467-025-63577-x

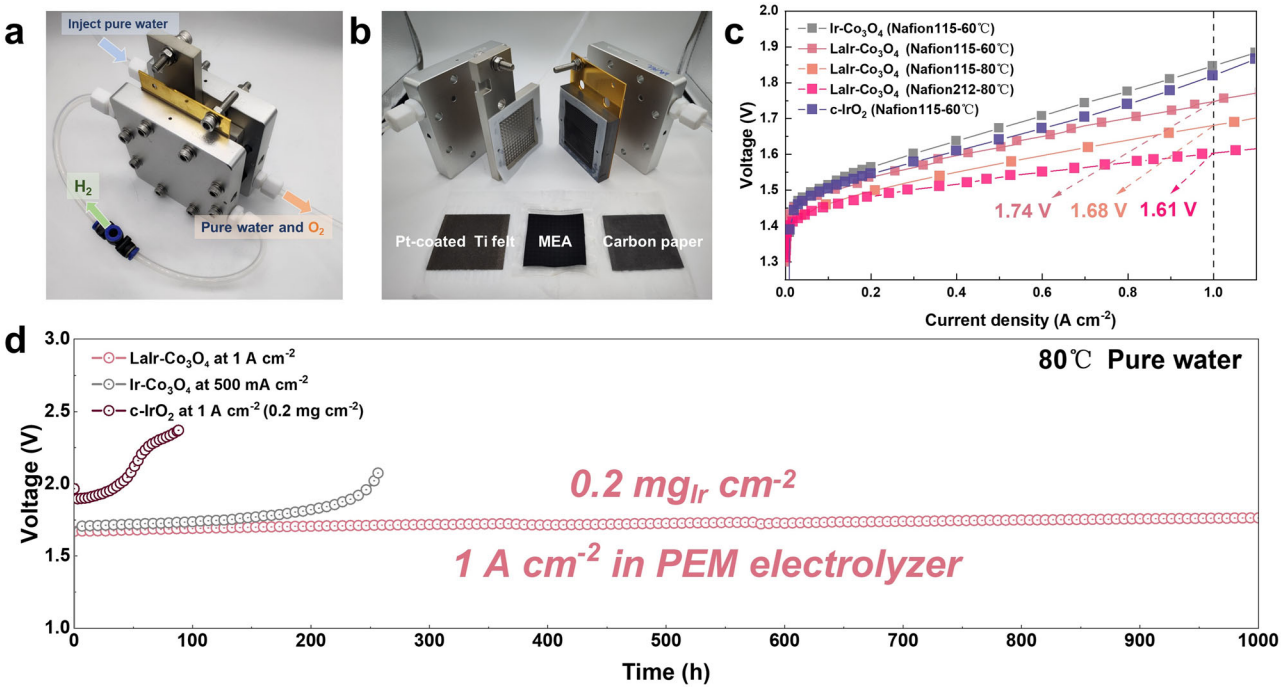

Fig. 7 | Electrochemical performances of LaIr-Co_3O_4 on PEMWE devices. Assembly (**a**) and disassembly (**b**) photos of the commercial PEM electrolyzer. **c** Polarization curves (without iR compensation) of the PEM electrolyzer with Ir-Co_3O_4, LaIr-Co_3O_4 and c-IrO_2. **d** Durability test of LaIr-Co_3O_4, Ir-Co_3O_4 and c-IrO_2 in the PEM-WE electrolyzer.

PEM-WE device performance

Bridging the gap between academic research and industry is critical to advancing promising PEM-WE technologies. It is indispensable for the performance testing of catalysts under simulated industrial conditions[19]. A PEM-WE system was built with catalyst coated membrane (CCM) type membrane electrode assembly (MEA) and cathode dry method (see details in Supplementary Information) to evaluate the actual operation of the catalyst (Fig. 7a, b). Implementing our LaIr-Co_3O_4 as an anode catalyst, notable PEM-WE performance was achieved with a small amount of Ir (0.2 mg_{Ir} cm^{-2}). As shown in Fig. 7c, the enhanced PEM-WE performance of LaIr-Co_3O_4 was pronounced at 1.0 A cm^{-2} and 60 °C compared with Ir-Co_3O_4 and commercial IrO_2. Specifically, our LaIr-Co_3O_4 achieved a much lower cell voltage of 1.74 V at 1.0 A cm^{-2} and 60 °C than that of Ir-Co_3O_4 (1.84 V) owing to improved activity of atomic level Ir species and metal-support interaction, and also superior to commercial IrO_2 (1.82 V). Assembled with Nafion212, our LaIr-Co_3O_4 could further achieve an extremely low cell voltages of 1.61 V at 1.0 A cm^{-2} and 80 °C.

In addition, the Ir-mass specific power is 5 mg_{Ir} kW^{-1} for LaIr-Co_3O_4 at 1.61 V. Such high mass power is attributed to the stable atomically dispersed Ir species on the LaIr-Co_3O_4 catalyst, which maintains higher atomic utilization and activity. From a commercial standpoint, these findings can be understood in terms of the Ir demand for a 10 GW facility. A current commercial PEM-WE deployment, operating at a specific power consumption of 0.75 g_{Ir} kW^{-1}, would typically require 7.5 tons of Ir for construction[49]. However, our results suggest that the Ir requirement for delivering a power of 10 GW can be reduced to just 0.05 tons, which represents only 0.7% of the annual global production of Ir. During an industrial-level current density of 1.0 A cm^{-1} stability test (Fig. 7d), LaIr-Co_3O_4 exhibits a competitive decay rate of −0.095 mV h^{-1}, significantly lower than that of Ir-Co_3O_4 (−2.24 mV h^{-1}) at 500 mA cm^{-1} and other Ir loaded acid OER catalysts reported in recent studies (Table S9). The high activity and stability of LaIr-Co_3O_4 in PEMWE were also significantly better than that of commercial iridium oxide (0.2 mg cm^{-1}), offering a promising way to realize low-iridium-loading catalyst applications.

To investigate the superior stability of LaIr-Co_3O_4, we compared HAADF-STEM and EDS results before and after the durability test in PEM-WE. The Ir single atoms in LaIr-Co_3O_4 remain anchored in the lattice after 500 h long-term operation at 500 mA cm^{-2}, allowing the Ir species to stay atomically dispersed even after prolonged electrolysis (as shown in Fig. S20), which is an important factor in maintaining the stability. Semi-quantitative EDS analysis (Table S8) also indicates that the dissolution loss of Ir elements is more significant in Ir-Co_3O_4 catalysts. After the 500 h test, the average rate of Ir dissolution in LaIr-Co_3O_4 is 0.054 wt.% h^{-1}. Ir-Co_3O_4 performance deteriorates significantly after 250 h of operation, primarily due to the instability of surface-absorbed Ir species. This instability leads further aggregation of Ir cluster (Fig. S21) and significant dissolution after a period of electrolysis. The average dissolution rate of Ir on Ir-Co_3O_4 is 0.11 wt.% h^{-1} from the result of EDS analysis (Table S8), which is much higher than that of LaIr-Co_3O_4. The highly maintained atomically dispersed Ir species and the reduced dissolution of Ir in LaIr-Co_3O_4 during the reaction are critical for maintaining both high activity and stability under PEM-WE operating conditions. This stability is closely linked to the unique coordination environment of lattice anchored type Ir single atoms and the stronger metal-support interaction discussed earlier. The Grazing Incidence X-ray Diffraction (GIXRD) measurements (fixed incidence angle: 2°) were performed on the MEA-anode after activation and following 500 h of continuous electrolysis in PEM electrolyzer (Fig. S22a). The GIXRD profiles exhibited two broad diffraction peaks at approximately 17.5° and 39° (2θ), consistent with the characteristic signals of the Nafion membrane as reported in prior studies[50,51]. While the pronounced background scattering from the Nafion membrane significantly attenuated the catalyst-derived signals, diffraction peaks corresponding to the (311), (400), and (400) crystallographic planes of Co_3O_4 were clearly resolved in the activated MEA. These peaks persisted in the post-operation MEA after 500 h of electrolysis at 1 A cm^{-2}, albeit with slightly reduced intensity. This attenuation could be attributed to minor dissolution or locally thinner catalytic layer. The retention of these crystallographic signatures demonstrates that the LaIr-Co_3O_4 catalyst maintains its structural integrity and phase stability

under industrial-relevant PEM electrolyzer conditions. Subsequently, complementary XPS characterization of the 500 h-operated MEA anode (Fig. S22b) revealed distinct F 1*s* peak from the Nafion membrane. Co 2*p* and Ir 4*f* peak can be also clearly observed that confirmed catalysts components in MEA after 500 h reaction. These results collectively confirm the dual retention of both Co_3O_4 spinel phases and anchored Ir species within the electrode assembly following prolonged operation in industrial PEMWE. More importantly, the preservation of characteristic metal speciation patterns under such harsh electrochemical conditions provides direct evidence for the robust structural integrity of this hybrid catalyst system.

Discussion

In summary, leveraging the stronger ion-exchange effect induced by La doping, we successfully prepared lattice anchored, atomically dispersed Ir in Co_3O_4. The incorporation of La optimizes the oxidation states of both the Co_3O_4 support and the Ir atoms, enhancing metal-support interaction. The lattice anchored Ir structure promotes the OPM reaction mechanism, resulting in significantly higher OER activity and stability compared to Ir-Co_3O_4 (surface-adsorbed Ir atomic species). Our LaIr-Co_3O_4 catalyst exhibited good PEM-WE activity, achieving 1.0 A cm^{-2} at a cell voltage of only 1.61 V, and demonstrated stable operation for over 1000 h at an industrial-level current density of 1.0 A cm^{-2}. Progressing toward precise anchoring of single-atom catalysts is crucial for realizing commercially viable low precious metal catalysts. Our doping-induced ion exchange method provides a guiding strategy for the design of more robust metal oxide-supported SACs.

Methods

Chemicals and materials

The chemicals including $Co(NO_3)_2{\cdot}6H_2O$ (≥99.9%), $La(NO_3)_3{\cdot}6H_2O$ (≥99.9%), Triethylamine (≥99%) 2-methylimidazole (≥98%), Water-^{18}O ($H_2{}^{18}O$, 97 at.% ^{18}O), 5% Nafion solution (Nafion® 117 solution) and carbinol (≥99.5%) were purchased from Aladdin. The commercial iridium dioxide (99.9%, powder) was purchased from Sigma-Aldrich. Carbon paper was obtained from SCI Materials Hub. Pt-coated porous Ti mesh was obtained from Sinero Technology Co., Ltd. All chemicals were used without further purification.

Synthesis of ZIF-67 nanocrystals

ZIF-67 nanocrystals were synthesized using a modified nucleation-growth separation method. Typically, 1 g of 2-methylimidazole and 1 ml of triethylamine (TEA) were dissolved in 30 ml of methanol to produce colorless solution A. Simultaneously, 0.882 g of $Co(NO_3)_2{\cdot}6H_2O$ was dissolved in 30 ml of methanol to create pink transparent solution B. Next, 1 ml of solution B was injected into solution A under ultrasonic conditions (53 Hz at 20 °C) and allowed to nucleate for 10 min. Subsequently, the remaining solution B was slowly added while maintaining ultrasonic conditions for an additional 10 min. The resulting purple precipitate was collected via centrifugation, washed thrice with ethanol, and dried under vacuum at 60 °C for approximately 12 h. To synthesize La-doped ZIF-67, the procedure remained mostly unchanged from that of ZIF-67, except for the introduction of lanthanum (La^{3+}) during synthesis. Specifically, 0.328 g $La(NO_3)_3{\cdot}6H_2O$ was added to solution B simultaneously with the other components to incorporate lanthanum into the ZIF structure.

Synthesis of Ir-Co_3O_4 and LaIr-Co_3O_4

Co_3O_4 and La-doped Co_3O_4 nanoparticle were first synthesized through the thermal decomposition of ZIF-67 and La-doped ZIF-67 precursor at 350 °C for 5 h with a ramp rate of 3 °C min^{-1} in muffle furnace respectively. The loading of atomic Ir species involved adding 0.0861 g iridium chloride to 30 ml deionized water and stirred to form a transparent solution. Following this, 200 mg of Co_3O_4 or La-doped Co_3O_4 were added in the solution and subjecting the mixture to continuous ultrasonication for 30 min. The resulting solution was then stirred for 8 h at 60 °C for ion exchange and subsequently washed with deionized water, centrifuged and transferred to a vacuum oven for drying and collection. Finally, the dried powder was subsequently transferred to a muffle furnace and heated at 200 °C for 2 h to obtain Ir-Co_3O_4 and LaIr-Co_3O_4.

Electrochemical measurements

Electrochemical measurements to evaluate the acidic-OER performance were conducted using a three-electrode setup in conjunction with the CHI760E workstation. The electrolyte is 0.5 M H_2SO_4 (pH = 0.3 ± 0.1) prepared by volumetric method and fresh electrolyte is used for each test. In this setup, platinum rods served as the counter electrode, an Ag/AgCl electrode was utilized as the reference electrode, and a 1 × 1 cm^2 piece of carbon paper (CP) supporting the catalysts functioned as the working electrode. Catalyst inks were prepared by mixing 6 mg of the catalyst in a solution containing 700 µl ethanol, 300 µl DI water and 10 µl 5 wt.% Nafion™ solution. Sonicating the mixture to form homogeneous solutions. Then, 200 µl of well-dispersed catalyst ink was sprayed onto a clean CP (1 × 1 cm^2) and dried to be tested. All the final potentials were converted to corresponding reference potentials of a RHE with the equation:

$$E(\text{vs.RHE}) = E\left(\text{vs.}\frac{\text{Ag}}{\text{AgCl}}\right) + 0.197\text{V} + 0.059 \times \text{pH} \quad (1)$$

Linear sweep voltammetry (LSV) curves of OER were obtained with a scan rate of 5 mV s^{-1} with iR correction. Electrochemical impedance spectroscopy (EIS) was performed at 1.53 V vs. RHE. The Nyquist plots for all samples were measured at the same potential value with an amplitude of 5 mV and frequencies ranging from 100 kHz to 0.1 Hz. Chronopotentiometric measurements were carried out at a current density of 10 mA cm^{-2} for 1000 h.

To determine the electrochemically active surface area (ECSA), cyclic voltammetry (CV) tests were conducted within the double-layer capacitance region, using a potential window between 1.1 and 1.2 V vs. RHE, at low scan rates ranging from 10 to 100 mV·s^{-1}. The specific double-layer capacitance (C_{dl}) was calculated using the following equation:

$$C_{dl} = \frac{\Delta j}{\upsilon} \quad (2)$$

where C_{dl}, v and Δj represents the specific double-layer capacitance, the scan rate and the half of the difference of andic and cathodic current density [($j_{anodic} - j_{cathodic}$)/2], respectively.

Turnover frequency (TOF) determination. The number of active sites is calculated using the following equation:

$$n_{Co} = \frac{Q_{Co}}{F} \times NA \quad (3)$$

where Q_{Co} is the integration area of redox peak from CV curves, *F* is the Faraday constant, *NA* is the Avogadro's constant, assuming that Co oxidation is a one-electro process.

The TOF value is calculated using the following equation:

$$TOF = \frac{J \times A \times \eta}{4 \times F \times n} \quad (4)$$

J is obtained at 1.60 V vs. RHE, normalized by geometric area, *A* is the geometric area, *F* is the Faraday constant and η is the Faradaic efficiency. n is the mole number of active atoms on the electrode, calculated from Eq. (3) above.

S-number calculation

The S-number proposed by Geiger et al.[12] is defined as the ratio between the number of moles of evolved oxygen (nO_2) and the number of moles of dissolved cobalt or iridium ($n_{Co/Ir}$)

$$S-number = \frac{n_{O_2(OER)}}{n_{Co/Ir}} \quad (5)$$

The number of moles of evolved oxygen was obtained by integrating the current (i in A during the respective potential hold

$$n_{O_2} = \frac{1}{zF}\int i(t)dt$$

where z is the number of moles of electrons transferred ($z = 4$ for the OER) and F is the Faraday constant (in C mol^{-1}). The number of moles of dissolved iridium was extracted from the iridium concentration ([Ir] in $\mu g\,L^{-1}$) measured by ICP.

$$n_{Co/Ir} = \frac{V}{M_{Co/Ir}}[Ir] \quad (7)$$

where V is the electrolyte volume and $M_{Co/Ir}$ is the molar mass of Co (58.9 g mol^{-1}) or Ir (192.2 g mol^{-1}).

PEM electrolyzer test

A membrane electrode assembly (MEA) with an active surface area of 25 cm^2 was used in a single-cell proton exchange membrane water electrolyzer (PEM-WE) with the catalyst-coated membrane (CCM) method. Nafion115 or Nafion212 served as the proton exchange membrane, pretreatment involving boiled sequentially for 60 min in 5 wt.% H_2O_2, 0.5 M H_2SO_4, and DI-water at 80 °C, followed by rinsing with deionized water after boiling in each solution. c-IrO_2, Ir-Co_3O_4 and LaIr-Co_3O_4 were employed as the anode catalysts respectively, while 75% Pt/C was used as the cathode catalyst. Homogeneous inks for both the anode and cathode were prepared, comprising the respective catalysts, Nafion solution (with a Nafion loading of 12 wt.% in the catalyst layer on both sides), isopropyl alcohol, and ultrapure water. The catalyst ink was subjected to ultrasonication in ice water for 2 h and subsequently sprayed onto both sides of the polymer membrane at 60 °C. The mass loadings were maintained at ~0.2 $mg_{Ir}\,cm^{-2}$ for the anode and ~0.5 $mg_{Pt}\,cm^{-2}$ for the cathode. A Pt-coated porous Ti mesh and carbon paper were used as porous transport layer (PTL) for the anode and cathode respectively. Electrolysis tests were conducted on a commercial single-cell PEM electrolyzer (Anhui Contango New Energy Technology Co.) with pre-heated DI-water fed into the anode side at a flow rate of 100 mL·min^{-1} and 60 °C or 80 °C. Tighten all the screw torque to 6 N in diagonal sequence during assemble. Before tests, the electrolyzer was activated by a polarized from 0 to 1.8 V_{cell} for 1000 cycles. All the cell voltages measured in PEM-WE electrolyzer were reported without applying iR compensation.

Materials characterization

The morphologies of catalysts were observed by SEM (SEM, HITACHI SU8600 S). X-ray diffraction (XRD) patterns as-obtained catalysts were performed on a Smart lab 9 kW in the range of 10° to 80°. High-resolution transmission electron microscopy (HRTEM) images and high-angle annular dark field scanning TEM (HAADF-STEM) images were collected on a Spectra Ultra transmission electron microscope operating at 200 kV. The elemental compositions were analyzed by inductively coupled plasma optical emission spectrometry (ICP-OES, Thermo Fisher ICAP PRO XP). The chemical valence state was collected by X-ray photoelectron spectroscopy (XPS, ESCALAB 250Xi).

XAS measurements

XAS spectra (including XANES and EXAFS) at the Co K-edge and Ir L_3-edge were collected at the BL11B beamline (Shanghai Synchrotron Radiation Facility) using Si(111) monochromators. Samples were pressed into thin sheets and sealed with Kapton tape. Data were recorded at room temperature in transmission mode (Co K-edge) or fluorescence mode (Ir L_3-edge) using a 4-element silicon drift detector (Bruker 5040). Negligible changes in the line-shape and peak position of Co K-edge XANES spectra were observed between two scans taken for a specific sample. Reference spectra (Co foil, Ir foil, CoO, Co_3O_4, IrO_2) were collected simultaneously for energy calibration. Data processing and EXAFS fitting were performed using Athena and Artemis software packages, with theoretical paths generated by FEFF6[52]. The energy calibration of the sample was conducted through standard and Co foil and Ir foil, which as a reference was simultaneously measured. A linear function was subtracted from the pre-edge region, then the edge jump was normalized using Athena software. The χ(k) data were isolated by subtracting a smooth, third-order polynomial approximating the absorption background of an isolated atom. The k_3-weighted χ(k) data were Fourier transformed after applying a HanFeng window function ($\Delta k = 1.0$). EXAFS fitting was performed in R-space using Artemis software. Structural parameters including coordination number (CN), bond distance (R), Debye-Waller factor (σ^2), and energy shift (ΔE_0) were optimized via nonlinear least-squares refinement of the EXAFS equation to the experimental data. The amplitude reduction factor (S_0^2) was constrained to values derived from reference foils (0.738 for Co; 0.746 for Ir) to ensure accurate CN determination for Co-O, Co-Co, Ir-O, and Ir-Co scattering paths.

Operando ATR-FTIR spectroscopy

Electrochemical in situ ATR-SEIRAS measurements were conducted using a Pike Veemax III ATR electrochemical cell equipped with a single reflection silicon crystal coated with an Au film, operating in internal reflection mode. The spectra were recorded on a Thermo Fisher Nicolet™ iS50 spectrometer. Working electrodes were prepared via sequential steps: (1) Chemical deposition of a ultrathin Au film onto a silicon ATR crystal to enhance surface plasmon resonance and electrical conductivity; (2) Drop-casting of catalyst ink (Nafion-free, 0.05 mg cm^{-2}) onto the Au-modified surface[53]. Subsequently, this silicon face-angled crystal was mounted on a spectro-electrochemical three-electrode cell, and a platinum wire and an Ag/AgCl electrode served as counter and reference electrodes, respectively. The Ar-saturated 0.5 M H_2SO_4 was used as the electrolyte for the OER test. The CP method was used in this experiment at different potentials (0.8–1.7 V vs. RHE, without iR correction).

Operando DEMS with isotope labeling

Operando differential electrochemical mass spectrometry (DEMS) experiments were performed using a Linglu instrument (QAS100). This setup includes two connected vacuum chambers: one housing the mass spectrometer under high vacuum and the other under mild vacuum, which connects directly to an electrochemical cell operating at ambient pressure. The pressure differential facilitates the downward movement of in-situ generated oxygen into the vacuum chamber for analysis, preventing its escape into the atmosphere. The working electrode is composed of a gold film sputtered onto a porous polytetrafluoroethylene (PTFE) membrane, which allows gas to pass while repelling liquid. A cold trap, cooled with dry ice, is installed between the electrochemical cell and the vacuum chamber to capture water vapor, protecting the mass spectrometer from potential damage. The catalyst ink is applied directly onto the gold film and subsequently dried. The electrochemical cell is configured as a standard three-electrode system. Isotope labeling experiments were conducted in a specified volume of N_2-saturated 0.5 M H_2SO_4 with $H_2{}^{18}O$ as solvent. The catalysts including LaIr-Co_3O_4 and Ir-Co_3O_4 were subjected to 5 LSV cycles within the potential range of 0.92–1.47 V vs. RHE at a scan rate of 5 mV s^{-1}. After labeling, the catalysts were washed with water ($H_2{}^{16}O$) to eliminate physically adhered $H_2{}^{18}O$ molecules, while the

leaving behind chemically bonded ^{18}O-containing species. The catalysts with isotope-labeled surface then operated in a normal electrolyte 0.5 M H_2SO_4 with $H_2{}^{16}O$ as solvent. Again, the gaseous products including $^{32}O_2$, $^{34}O_2$ and $^{36}O_2$ were monitored by the mass spectrometer during 5 LSV cycles in the potential range of 0.92–1.47 V vs. RHE at a scan rate of 5 mV s^{-1}.

Computational details

All spin-polarized DFT calculations in the work were performed using the Vienna ab initio simulation program (VASP)[54,55] with the projector-augmented wave (PAW) pseudopotentials method[55,56]. The electronic structures were computed within the generalized gradient approximation (GGA) using the Perdew–Burke–Ernzerhof (PBE) functional[57], expanded in a plane-wave basis set[54,58] with a cut-off energy of 450 eV. To account for the strong electron correlations in the Co 3 *d* orbitals, the Hubbard-*U* correction with a *U-J* term of 3.5 eV was applied. A 2 × 2 × 1 Monkhorst–Pack k-point mesh sampling was employed for surface optimization, while van der Waal (vdW) interactions were incorporated using the DFT-D3 method[59,60]. Transition states (TSs) were located using a constrained minimization technique[61–63]. Structural relaxations were considered converged when the forces on all atoms fell below 0.05 eV/Å and the self-consistent energy differences were less than 10^{-5} eV. The surface models included a $p(1\times1)$ Co_3O_4 (311) surface and a $p(\sqrt{2}\times\sqrt{2})$ Co_3O_4 (100) surface, each with four atomic layers, as well as a $p(1\times1)$ Co_3O_4 (110) surface with six atomic layers. In all cases, the bottom two layers were fixed to mimic the bulk phase, while the other layers were fully relaxed. A vacuum layer of 10 Å was introduced to eliminate periodic interactions between adjacent slabs. To construct the LaIr-Co_3O_4 surfaces, the most stable configurations of La-anchored Co_3O_4 (311), (100), and (110) facets were first identified. Subsequently, the LaIr-Co_3O_4 surfaces were modeled by substituting La^{3+} with Ir^{3+} at the same site (Fig. S23). The Ir-Co_3O_4 (311) surface was constructed by adsorbing an Ir atom onto the Co_3O_4 (311) surface. The atomic coordinates of the optimized computational models are provided in Supplementary Data 1. The isolated ions (Co^{3+}, Ir^{3+}, La^{3+}) were simulated using Gaussian16 with the B3LYP functional and the LANL2DZ basis set to ensure reliable calculations of electronic properties.

The substitution reactions of Ir^{3+} for La^{3+} or Co^{3+} are shown below:

$$Co_{(3-x)}La_xO_4 + yIr^{3+} \rightarrow Co_{(3-x)}La_{(x-y)}Ir_yO_4 + yLa^{3+} \quad \text{(S1)}$$

$$Co_3O_4 + yIr^{3+} \rightarrow Co_{(3-y)}Ir_yO_4 + yCo^{3+} \quad \text{(S2)}$$

The corresponding reaction energies (ΔE) for Eqs. (1) and (2) were calculated as:

$$\Delta E_1 = yE_{La^{3+}} + E_{Co_{(3-x)}La_{(x-y)}Ir_yO_4} - yE_{Ir^{3+}} - E_{Co_{(3-x)}La_xO_4} \quad \text{(S3)}$$

$$\Delta E_2 = yE_{Co^{3+}} + E_{Co_{(3-y)}Ir_yO_4} - yE_{Ir^{3+}} - E_{Co_3O_4} \quad \text{(S4)}$$

where E_n is the electronic energy of species n obtained directly from DFT simulation. The Gibbs free energy (ΔG) for adsorbed intermediates can be expressed as:

$$\Delta G = \Delta E + \Delta ZPE - T\cdot\Delta S \quad \text{(S5)}$$

where ΔE is the reaction energy calculated using DFT methods. ΔZPE is the zero-point energy correction, and $T\Delta S$ represents the entropic contribution at 298.15 K, evaluated from the vibrational partition function.

Data availability

The data that support the conclusions of this study are available within the paper and Supplementary information. Source data are provided with this paper.

References

1. Turner, J. A. Sustainable hydrogen production. *Science* **305**, 972–974 (2004).
2. Zhang, K. et al. Status and perspectives of key materials for PEM electrolyzer. *Nano Res. Energy* **1**, e9120032 (2022).
3. Mayyas, A. T. et al. Manufacturing cost analysis for proton exchange membrane water electrolyzers.). (National Renewable Energy Lab. (NREL), Golden, CO (United States), 2019).
4. Su, H. et al. Tensile straining of iridium sites in manganese oxides for proton-exchange membrane water electrolysers. *Nat. Commun.* **15**, 95–106 (2024).
5. Zhang, Z. R. et al. Distance effect of single atoms on stability of cobalt oxide catalysts for acidic oxygen evolution. *Nat. Commun.* **15**, 1767–1776 (2024).
6. Lee, J. K. et al. Nanochannel electrodes facilitating interfacial transport for PEM water electrolysis. *Joule* **8**, 2357–2373 (2024).
7. Maulana, A. L. et al. Understanding the structural evolution of IrFeCoNiCu high-entropy alloy nanoparticles under the acidic oxygen evolution reaction. *Nano Lett.* **23**, 6637–6644 (2023).
8. Jiang, G. et al. An effective oxygen electrode based on $Ir_{0.6}Sn_{0.4}O_2$ for PEM water electrolyzers. *J. Energy Chem.* **39**, 23–28 (2019).
9. Tran, N. Q. et al. Low iridium content confined inside a Co_3O_4 hollow sphere for superior acidic water oxidation. *ACS Sustain. Chem. Eng.* **7**, 16640–16650 (2019).
10. Pham, C. V. et al. IrO_2 coated TiO_2 core-shell microparticles advance performance of low loading proton exchange membrane water electrolyzers. *Appl Catal. B* **269**, 118762–118774 (2020).
11. Li, A. et al. Atomically dispersed hexavalent iridium oxide from MnO_2 reduction for oxygen evolution catalysis. *Science* **384**, 666–670 (2024).
12. Geiger, S. et al. The stability number as a metric for electrocatalyst stability benchmarking. *Nat. Catal.* **1**, 508–515 (2018).
13. Wu, Q. et al. Advances and status of anode catalysts for proton exchange membrane water electrolysis technology. *Mater. Chem. Front.* **7**, 1025–1045 (2023).
14. Shi, Z. et al. Confined Ir single sites with triggered lattice oxygen redox: toward boosted and sustained water oxidation catalysis. *Joule* **5**, 2164–2176 (2021).
15. Lin, H. Y. et al. Enriched oxygen coverage localized within Ir atomic grids for enhanced oxygen evolution electrocatalysis. *Adv. Mater.* **36**, 2408045 (2024).
16. Suhadolnik, L. et al. Nanotubular TiO_xN_y-supported Ir single atoms and clusters as thin-film electrocatalysts for oxygen evolution in acid media. *Chem. Mater.* **35**, 2612–2623 (2023).
17. Yin, J. et al. Iridium single atoms coupling with oxygen vacancies boosts oxygen evolution reaction in acid media. *J. Am. Chem. Soc.* **142**, 18378–18386 (2020).
18. Hua, K. et al. Integrating atomically dispersed Ir sites in $MnCo_2O_{4.5}$ for highly stable acidic oxygen evolution reaction. *ACS Catal.* **14**, 3712–3724 (2024).
19. Tao, H. B. et al. The gap between academic research on proton exchange membrane water electrolysers and industrial demands. *Nat. Nanotechnol.* **19**, 1074–1076 (2024).
20. Kaushik, S. et al. Universal synthesis of single-atom catalysts by direct thermal decomposition of molten salts for boosting acidic water splitting. *Adv. Mater.* **36**, 2401163 (2024).
21. Liu, J.-C. et al. Theoretical understanding of the stability of single-atom catalysts. *Natl Sci. Rev.* **5**, 638–641 (2018).

22. Qi, K., Chhowalla, M. & Voiry, D. Single atom is not alone: metal–support interactions in single-atom catalysis. *Mater. Today* **40**, 173–192 (2020).
23. Qin, R., Liu, P., Fu, G. & Zheng, N. Strategies for stabilizing atomically dispersed metal catalysts. *Small Methods* **2**, 1700286 (2017).
24. Robb, D. T. & Privman, V. Model of nanocrystal formation in solution by burst nucleation and diffusional growth. *Langmuir* **24**, 26–35 (2008).
25. Chong, L. et al. La-and Mn-doped cobalt spinel oxygen evolution catalyst for proton exchange membrane electrolysis. *Science* **380**, 609–616 (2023).
26. Lee, K. et al. Tailoring cobalt spinel oxide with site-specific single atom incorporation for high-performance electrocatalysis. *Energy Environ. Sci.* **17**, 3618–3628 (2024).
27. Shan, J. et al. Short-range ordered iridium single atoms integrated into cobalt oxide spinel structure for highly efficient electrocatalytic water oxidation. *J. Am. Chem. Soc.* **143**, 5201–5211 (2021).
28. Zhu, W. et al. Direct dioxygen radical coupling driven by octahedral ruthenium–oxygen–cobalt collaborative coordination for acidic oxygen evolution reaction. *J. Am. Chem. Soc.* **145**, 17995–18006 (2023).
29. Hao, Y. et al. Switching the oxygen evolution mechanism on atomically dispersed Ru for enhanced acidic reaction kinetics. *J. Am. Chem. Soc.* **145**, 23659–23669 (2023).
30. Zhu, Y. et al. Iridium single atoms incorporated in Co_3O_4 efficiently catalyze the oxygen evolution in acidic conditions. *Nat. Commun.* **13**, 7754 (2022).
31. Feng, H. L. et al. Room-temperature ferrimagnetism of anti-site-disordered Ca_2MnOsO_6. *Phys. Rev. Mater.* **3**, 124404 (2019).
32. Agrestini, S. et al. Nature of the magnetism of iridium in the double perovskite Sr_2CoIrO_6. *Phys. Rev. B* **100**, 014443 (2019).
33. Cao, J. et al. Tungsten single atoms incorporated in cobalt spinel oxide for highly efficient electrocatalytic oxygen evolution in acid. *Energy Environ. Sci.* **17**, 5911–5921 (2024).
34. Chang, J. W. et al. Oxygen radical coupling on short-range ordered Ru atom arrays enables exceptional activity and stability for acidic water oxidation. *J. Am. Chem. Soc.* **146**, 12958–12968 (2024).
35. Anantharaj, S. & Noda, S. Appropriate use of electrochemical impedance spectroscopy in water splitting electrocatalysis. *ChemElectroChem* **7**, 2297–2308 (2020).
36. Abbou, S. et al. Manipulating the corrosion resistance of SnO2 aerogels through doping for efficient and durable oxygen evolution reaction electrocatalysis in acidic media. *ACS Catal.* **10**, 7283–7294 (2020).
37. Daiane Ferreira da Silva, C. et al. Oxygen evolution reaction activity and stability benchmarks for supported and unsupported IrOx electrocatalysts. *ACS Catal.* **11**, 4107–4116 (2021).
38. Knöppel, J. et al. On the limitations in assessing stability of oxygen evolution catalysts using aqueous model electrochemical cells. *Nat. Commun.* **12**, 2231 (2021).
39. Kwon, J. et al. Tailored electronic structure of Ir in high entropy alloy for highly active and durable bifunctional electrocatalyst for water splitting under an acidic environment. *Adv. Mater.* **35**, e2300091 (2023).
40. Chen, Y. et al. Exceptionally active iridium evolved from a pseudo-cubic perovskite for oxygen evolution in acid. *Nat. Commun.* **10** (2019).
41. Lin, C. et al. In-situ reconstructed Ru atom array on α-MnO_2 with enhanced performance for acidic water oxidation. *Nat. Catal.* **4**, 1012–1023 (2021).
42. Lang, C. et al. Observation of a potential-dependent switch of water-oxidation mechanism on Co-oxide-based catalysts. *Chem* **7**, 2101–2117 (2021).
43. Wang, B. et al. In situ structural evolution of the multi-site alloy electrocatalyst to manipulate the intermediate for enhanced water oxidation reaction. *Energy Environ. Sci.* **13**, 2200–2208 (2020).
44. Qin, Y. et al. RuO_2 electronic structure and lattice strain dual engineering for enhanced acidic oxygen evolution reaction performance. *Nat. Commun.* **13**, 3784 (2022).
45. Lu, Q. et al. Breaking the activity-stability trade-off of RuO_2 via metallic Ru bilateral regulation for acidic oxygen evolution reaction. *Angew. Chem. Int. Ed.***64**, e202503733 (2025).
46. Huang, Z.-F. et al. Chemical and structural origin of lattice oxygen oxidation in Co–Zn oxyhydroxide oxygen evolution electrocatalysts. *Nat. Energy* **4**, 329–338 (2019).
47. Yin, Z.-H., Liu, H., Hu, J.-S. & Wang, J.-J. The breakthrough of oxide pathway mechanism in stability and scaling relationship for water oxidation. *Natl Sci. Rev.* **11**, nwae362 (2024).
48. Wang, Q. et al. Lattice-doped Ir cooperating with surface-anchored IrO_x for acidic oxygen evolution reaction with ultralow Ir loading. *ACS Appl. Mater. Interfaces* **17**, 7929–7937 (2025).
49. Kim, M.-G. et al. Iridium selenium oxyhydroxide shell for polymer electrolyte membrane water electrolyzer with low Ir loading. *ACS Energy Lett.* **9**, 2876–2884 (2024).
50. Sigwadi, R. et al. The proton conductivity and mechanical properties of Nafion®/ ZrP nanocomposite membrane. *Heliyon* **5**, e02240 (2019).
51. Cele, N. & Ray, S. S. Recent progress on Nafion-based nanocomposite membranes for fuel cell applications. *Macromol. Mater. Eng.* **294**, 719–738 (2009).
52. Ravel, B. & Newville, M. ATHENA, ARTEMIS, HEPHAESTUS: data analysis for X-ray absorption spectroscopy using IFEFFIT. *J. Synchrotron Radiat.* **12**, 537–541 (2005).
53. Liu, H. et al. Eliminating over-oxidation of ruthenium oxides by niobium for highly stable electrocatalytic oxygen evolution in acidic media. *Joule* **7**, 558–573 (2023).
54. Kresse, G. & Furthmüller, J. Efficient iterative schemes for ab initio total-energy calculations using a plane-wave basis set. *Phys. Rev. B* **54**, 11169–11186 (1996).
55. Kresse, G. & Joubert, D. From ultrasoft pseudopotentials to the projector augmented-wave method. *Phys. Rev. B* **59**, 1758–1775 (1999).
56. Blöchl, P. E. Projector augmented-wave method. *Phys. Rev. B* **50**, 17953–17979 (1994).
57. Perdew, J. P., Burke, K. & Ernzerhof, M. Generalized gradient approximation made simple. *Phys. Rev. Lett.* **77**, 3865–3868 (1996).
58. Kresse, G. & Furthmüller, J. Efficiency of ab-initio total energy calculations for metals and semiconductors using a plane-wave basis set. *Comput. Mater. Sci.* **6**, 15–50 (1996).
59. Grimme, S., Antony, J., Ehrlich, S. & Krieg, H. A consistent and accurate Ab Initio parametrization of density functional dispersion correction (DFT-D) for the 94 elements H-Pu. *J. Chem. Phys.* **132**, 154104 (2010).
60. Grimme, S., Ehrlich, S. & Goerigk, L. Effect of the damping function in dispersion corrected density functional theory. *J. Comput. Chem.* **32**, 1456–1465 (2011).
61. Michaelides, A. & Hu, P. Catalytic water formation on platinum: a first-principles study. *J. Am. Chem. Soc.* **123**, 4235–4242 (2001).
62. Liu, Z. P. & Hu, P. General rules for predicting where a catalytic reaction should occur on metal surfaces: a density functional theory study of C-H and C-O bond breaking/making on flat, stepped, and kinked metal surfaces. *J. Am. Chem. Soc.* **125**, 1958–1967 (2003).
63. Alavi, A. et al. CO oxidation on Pt (111): an ab initio density functional theory study. *Phys. Rev. Lett.* **80**, 3650–3653 (1998).

Acknowledgements

This work is financially supported by the National Natural Science Foundation of China (22279105), the National Key R&D Program of China (2022YFC3401802), the Zhejiang Provincial Natural Science Foundation (XHD24B0201), the starting-up package from Westlake University, Research Center for Industries of the Future, and Zhejiang Baima Lake

Laboratory. We thank the Center of Artificial Photosynthesis (CAP) for Solar Fuels at Westlake University for academic and instrument support. We thank the Instrumentation and Service Center for Physical Sciences (ISCPS) and the Instrumentation and Service Center for Molecular Sciences (ISCMS) at Westlake University for the facility support and technical assistance, and Westlake University HPC Center for computation support.

Author contributions

B.-B.Z. supervised this project. Z.-M.W. designed and performed research; Y.-X.D. supervised and carried out DFT calculations and wrote part of paper; Z.-M.W. wrote the first draft of the paper; B.-B.Z. revised and edited the manuscript, funding acquisition, project administration. Q.-K.J performed aberration-corrected transmission electron microscopy. W.-L.S. contributed to PEM testing. F.-Y.Z., Y.-X.S., X. C., Y. G. and L.-C. S. participated in discussions and manuscript proofreading.

Competing interests

The authors declare no competing interests.

Additional information

Supplementary information The online version contains supplementary material available at https://doi.org/10.1038/s41467-025-63577-x.

Correspondence and requests for materials should be addressed to Yunxuan Ding or Biaobiao Zhang.

Peer review information *Nature Communications* thanks the anonymous reviewers for their contribution to the peer review of this work. A peer review file is available.